Ultra-broadband nanophotonic beamsplitter using an anisotropic sub-wavelength metamaterial

Halir, Robert; Cheben, Pavel; Luque-González, José manuel; Sarmiento-merenguel, Jose darío; Schmid, Jens H.; Wangüemert-pérez, Gonzalo; Xu, Dan-xia; Wang, Shurui; Ortega-moñux, Alejandro; Molina-fernández, Íñigo

Publisher's version / Version de l'éditeur:
https://doi.org/10.1002/lpor.201600213
Laser and Photonics Reviews, 10, 6, pp. 1039-1046, 2016-11-22

LASER
& PHOTONICS
REVIEWS

Laser Photonics Rev. **10,** No. 6, 1039–1046 (2016) / **DOI** 10.1002/lpor.201600213

Abstract Nanophotonic beamsplitters are fundamental building blocks in integrated optics, with applications ranging from high speed telecom receivers to biological sensors and quantum splitters. While high-performance multiport beamsplitters have been demonstrated in several material platforms using multimode interference couplers, their operation bandwidth remains fundamentally limited. Here, we leverage the inherent anisotropy and dispersion of a sub-wavelength structured photonic metamaterial to demonstrate ultra-broadband integrated beamsplitting. Our device, which is three times more compact than its conventional counterpart, can achieve high-performance operation over an unprecedented 500 nm design bandwidth exceeding all optical communication bands combined, and making it one of the most broadband silicon photonics components reported to date. Our demonstration paves the way toward nanophotonic waveguide components with ultra-broadband operation for next generation integrated photonic systems.

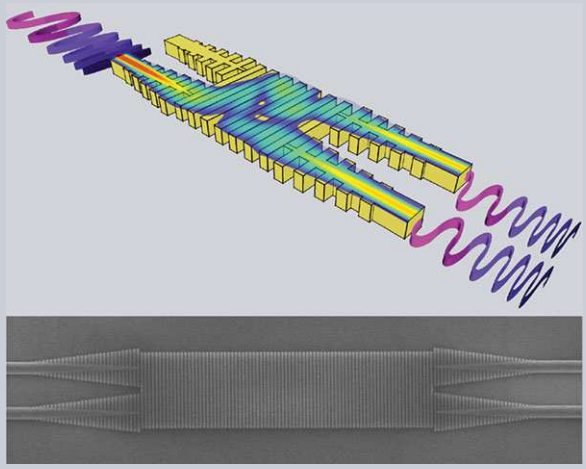

ORIGINAL
PAPER

Ultra-broadband nanophotonic beamsplitter using an anisotropic sub-wavelength metamaterial

Robert Halir[1,2,*], Pavel Cheben[3], José Manuel Luque-González[1], Jose Darío Sarmiento-Merenguel[1], Jens H. Schmid[3], Gonzalo Wangüemert-Pérez[1], Dan-Xia Xu[3], Shurui Wang[3], Alejandro Ortega-Moñux[1,2], and Íñigo Molina-Fernández[1,2]

1. Introduction

Integrated photonic systems are poised to produce key advances in areas such as optical communications [1,2], sensing [3, 4], spectroscopy [5, 6], metrology [7], frequency comb generation [8] and quantum physics [9, 10]. Since beamsplitters are fundamental photonic building blocks, substantially extending their operational bandwidth would pave the way towards broadband systems capable, for instance, of covering several optical communication bands, or realizing sensors and frequency combs over large spectral regions as required in optical coherence tomography. Integrated beamsplitters are preferably implemented with multimode interference couplers (MMIs), which exploit the self-imaging effect discovered by Henry Talbot in the 1830s [11]. Talbot imaging allows to form multiport couplers with well defined amplitude and phase ratios that offer improved performance compared to y-branches and directional couplers [12, 13]. MMI couplers are used in a wide variety of waveguide devices [1, 10, 14–18], and have been implemented in a broad range of material platforms [19–22]. However, until very recently, the same classical structure, similar to the one shown in Fig. 1 for a 2×2 MMI configuration, has been used. Consisting of an essentially rectangular central multimode region with tapered input and output waveguides, it provides a rugged design, but also imposes fundamental restrictions in terms of size and bandwidth [13,23]. On the other hand, sub-wavelength structures have been proposed for achromatic free space optics in the past [24]. The more recent advent of sub-wavelength grating (SWG) integrated waveguides has enabled the concept of on-chip refractive index engineering [25,26]. This idea has ushered in breakthrough devices for fiber-to-chip coupling [27, 28], wavelength multiplexing [29], and polarization splitting [30], among other innovations. Applied to MMIs, sub-wavelength index engineering led to the first demonstration of a slotted MMI [31], which reduced the size of the device by a factor of two compared to a conventional MMI, without affecting its performance.

Building on our exploratory simulation work in [32], here we report on the design and first ever experimental demonstration of an ultra-broadband MMI [see Fig. 2(a)].

[1] Universidad de Málaga, Dept. de Ingeniería de Comunicaciones, ETSI Telecomunicación, Campus de Teatinos s/n, 29071 Málaga, España
[2] Bionand Center for Nanomedicine and Biotechnology, Parque Tecnológico de Andalucía, 29590 Málaga, España
[3] National Research Council of Canada, Ottawa, Ontario, K1A 0R6, Canada
*Corresponding author: e-mail: robert.halir@ic.uma.es

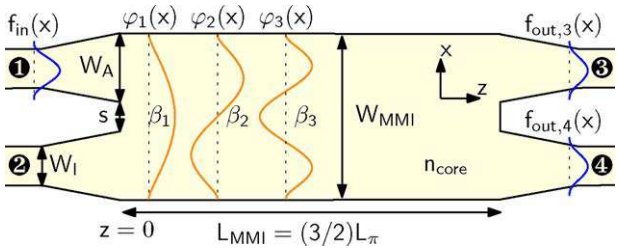

Figure 1 Schematic 2D model of a 2 × 2 MMI. When the mode of the input waveguide, $f_{in}(x)$, is launched into the multimode region it excites several higher order modes, $\varphi_i(x)$, which interfere forming Talbot-type self-images of the input field. Coupling of these self-images to the output waveguide yields the output fields $f_{out,3}(x)$ and $f_{out,4}(x)$, each carrying half of the input power with a relative phase shift of 90°.

We describe self-imaging in an effectively anisotropic sub-wavelength structure, providing deep physical insight into the operation of the device alongside an analytic design expression. In combination with dispersion engineering, this enables us to demonstrate a MMI that yields a threefold size reduction compared to a conventional device, while at the same time experimentally achieving high performance (excess losses and imbalance < 1 dB, phase error < 5°) over an unprecedented bandwidth of more than 300 nm around a central wavelength of 1.55 μm, limited by our measurement setup. Full 3D simulations predict the bandwidth exceeding 500 nm; in simulation an optimized conventional MMI design covers less than 200 nm with comparable performance. To the best of our knowledge this not only constitutes the MMI with the broadest bandwidth ever demonstrated, but also one of the most broadband, fully passive integrated optical devices in general.

2. Self-imaging revisited

We first focus on the 2D schematic of the MMI shown in Fig. 1 and 2(a) to give a general description of the self-imaging effect in conventional and sub-wavelength engineered MMIs. In both devices the mode field launched from the input waveguide, $f_{in}(x)$, is expanded into the modes of the multimode slab region, i.e. $f_{in}(x) = \sum_m c_m \varphi_m(x)$, with c_m the overlap between the input field and the m-th slab mode. These modes propagate with specific phase constants, β_m, producing self-images of the input field as they interfere. The positions at which these images form is governed by the beat length of the two lowest order modes [13],

$$L_\pi = \frac{\pi}{\beta_1 - \beta_2}. \tag{1}$$

For instance, a double image of the input field is formed at $z = \frac{3}{2}L_\pi = L_{MMI}$, where L_{MMI} is the physical length of the multimode region (see Fig. 1). Since L_{MMI} is fixed, any wavelength variation of the beat length will result in a detuning of the device and in a significant degradation of its performance.

2.1. Conventional multimode interference

In a conventional MMI, under the paraxial approximation, the beat length is given by

$$L_\pi^{conv} \approx \frac{4W_e^2}{3\lambda} n_{core}, \tag{2}$$

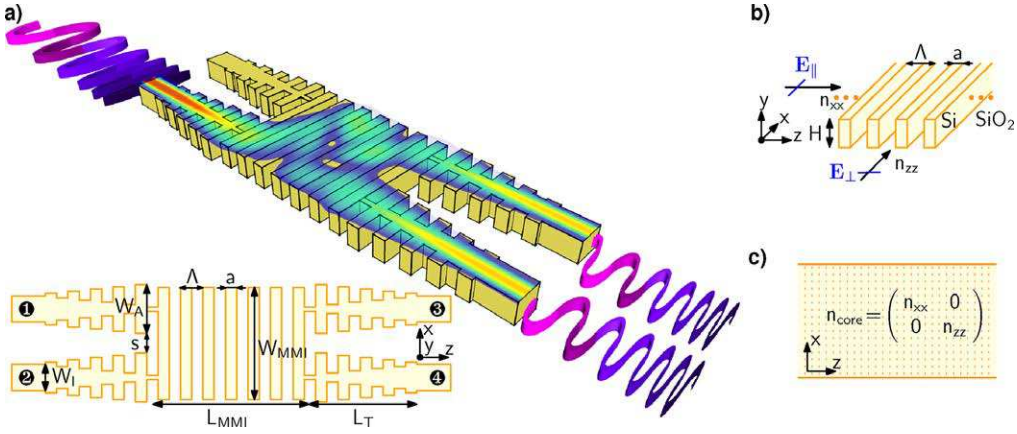

Figure 2 a) Ultra-broadband multimode interference coupler. The central multimode region is segmented at a sub-wavelength scale to engineer the waveguide anisotropy and dispersion, achieving a beat length that is virtually independent of wavelength. The sub-wavelength grating tapered input and output waveguides ensure efficient coupling with the silicon wire interconnecting waveguides. In the illustration TE polarized light (electric field along the x-axis) with varying wavelength is injected into one of the input ports and is split among the two output waveguides with equal amplitude and a 90° phase shift. b) The anisotropy of the sub-wavelength structure becomes apparent by considering the propagation of waves with their electric fields parallel ($E_\parallel$) and perpendicular ($E_\perp$) to the interfaces. c) The sub-wavelength structure can be modeled through a 2D anisotropic material described by an effective index tensor.

Table 1 Geometrical parameters of the conventional and the broadband MMI shown in Fig. 1 and 2(a), respectively.

Parameter	Conventional	Broadband
Silicon thickness (H)	220 nm	
Width MMI (W_{MMI})	3.25μm	
Length MMI (L_{MMI})	38.5 μm	14 μm
		74 periods
Width input (W_I)	0.5 μm	
Width access (W_A)	1.7 μm	
Length taper (L_T)	6 μm	5.7 μm
		30 periods
Separation (s)	0.3 μm	
Period (Λ)	–	190 nm
Duty-cycle (DC)	–	50 %

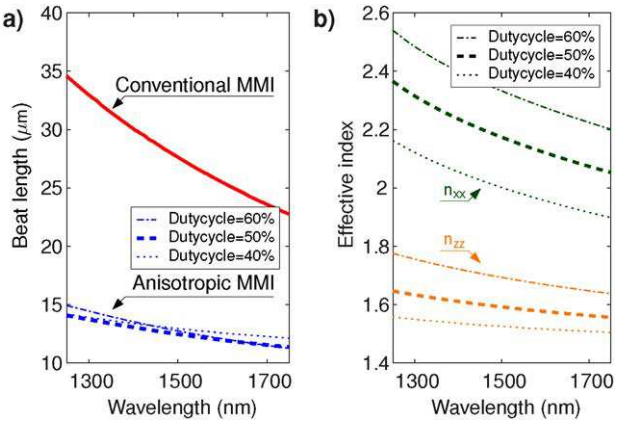

Figure 3 a) Semi-analytic calculation of the beat length of a conventional MMI device and the sub-wavelength engineered MMI modeled through the anisotropic medium $n_{core} = \mathrm{diag}[n_{xx}, n_{zz}]$. The anisotropy of the sub-wavelength engineered MMI yields an almost threefold reduction in beat length compared to the conventional MMI, as well as a substantially reduced wavelength dependence. b) Anisotropic effective indexes of the sub-wavelength grating metamaterial shown in Fig. 2(b) as a function of wavelength and duty-cycle for the dimensions given in table 1.

where n_{core} is the effective index of the multimode region (for TE polarization in our case) obtained with the effective index method [33] and λ is the free space wavelength. W_e is the effective width of the multimode region taking into account the Goos-Hänchen shift, which is assumed to be identical for all modes and invariant with wavelength [13]. The choice of the material platform clearly dictates the value of n_{core} and its wavelength dependence. The minimum width of the multimode region is determined by the separation (s) between the input/output waveguides, to avoid coupling between them, and the required width of the access waveguides (W_A), to control the excitation of higher order modes; see [15,34] for details. Hence, there is very limited freedom to engineer the beat length or its wavelength dependence.

Considering a $H = 220\,\mathrm{nm}$ thick silicon platform with silicon dioxide (SiO_2) upper cladding, TE polarization, and the geometrical parameters given in table 1, we have $n_{\mathrm{core}} \sim 2.87$, so that Eq. (2) yields $L_\pi^{\mathrm{conv}} \approx 27\,\mu\mathrm{m}$ at $\lambda = 1500\,\mathrm{nm}$. Figure 3(a) shows the beat length calculated through Eq. (1), with $\beta_{1,2}$ obtained from a slab waveguide of width W_{MMI}, silicon dioxide cladding, and effective core index n_{core}. The beat length is $L_\pi^{\mathrm{conv}} \sim 28\,\mu\mathrm{m}$ at $\lambda = 1500\,\mathrm{nm}$, in good agreement with Eq. (2). However, due to the strong wavelength dependence, the device will only operate in a limited bandwidth of $\sim 200\,\mathrm{nm}$ as discussed below.

2.2. Multimode interference in segmented media

2.2.1. Effective index of the sub-wavelength structured multimode region

The fundamental advantage of our broadband MMI device, shown in Fig. 2(a), arises from the inherent anisotropy of its sub-wavelength structure. This anisotropy is well-known in crystal optics, where uniaxial crystals are modelled as anisotropic media described by an index tensor $\mathrm{diag}[n_o, n_o, n_e]$, with n_o and n_e the ordinary and extraordinary refractive index, respectively [35–37].

In order to incorporate the effect of the sub-wavelength structure into the classical 2D MMI model discussed in the previous sections, we first need to establish its effective index, n_{core}. We achieve this by extending the classical effective index method (EIM) for the TE (in-plane) polarization state of interest. In analogy with the classical EIM, we start by infinitely extending the segmented waveguide in the x and z direction, as illustrated in Fig. 2(b). Note that for a non-segmented waveguide, where $a = \Lambda$, this structure is simply an isotropic slab waveguide, and n_{core} is given by the effective index of the fundamental TE (in-plane) slab mode. However, in the segmented structure, two distinct fundamental modes can be supported: i) the fundamental Bloch mode traveling in the z direction and polarized along the x axis ($E_\parallel$), with effective index n_{xx}; ii) the fundamental waveguide-array mode traveling in the x direction and polarized along the z axis ($E_\perp$), with effective index n_{zz}. As expected, the 2D equivalent medium is thus anisotropic and the desired effective index is a tensor: $\boldsymbol{n_{core}} = \mathrm{diag}[n_{xx}, n_{zz}]$, as illustrated in Fig. 2(c). From a physical point of view this means that in the effective medium in Fig. 2(c) the displacement field $\boldsymbol{D}$ and the electric field $\boldsymbol{E}$ are related as $\boldsymbol{D} = \varepsilon_0 \boldsymbol{n}_{\boldsymbol{core}}^2 \boldsymbol{E}$, with ε_0 the vacuum permittivity. A description of the simulation tools used to calculate n_{xx} and n_{zz} is available in the supporting information.

2.2.2. Calculation of the beat length

Having established a homogeneous 2D model of the sub-wavelength structure, we can now find analytical expressions for the propagation constants (β_m) of the

modes in the MMI multimode section, which in turn yield the approximate beat length. Extending the procedure outlined in [13] for conventional isotropic MMIs we find that in the anisotropic case the beat length is given by:

$$L_\pi^{\text{aniso}} \approx \frac{4W_e^2}{3\lambda}\frac{n_{zz}^2}{n_{xx}}. \quad (3)$$

Equation (3) provides an analytical design framework for our ultra-broadband MMIs. The specifics of the derivation are provided in the supporting information.

Figure 3(b) shows the effective indices n_{xx} and n_{zz} as function of wavelength and duty-cycle for the dimensions of the sub-wavelength structure given in table 1. Specifically at $\lambda = 1500\,\text{nm}$ and for a duty-cycle of 50 % we have $n_{xx} \sim 2.15$, $n_{zz} \sim 1.6$. Equation (3) then predicts a significantly reduced beat length of $L_\pi^{\text{aniso}} \approx 11.5\,\mu\text{m}$, which arises directly from the reduced value of $n_{zz}^2/n_{xx} \sim 1.2$ compared to $n_{\text{core}} \sim 2.87$ [see Eqs. (2) and (3)]. Since the variation of L_π^{aniso} and L_π^{conv} with wavelength is, to first order, proportional to n_{zz}^2/n_{xx} and n_{core}, the wavelength dependence of the beat length is also expected to decrease. Furthermore, the increase of n_{xx} with decreasing wavelength [Fig. 3(b)] cancels part of the wavelength (λ) term in Eq. (3). Figure 3(a) shows the beat length calculated through Eq. (1), with $\beta_{1,2}$ obtained from an anisotropic slab waveguide of width W_{MMI}, silicon dioxide cladding, and $\boldsymbol{n_{core}} = \text{diag}[n_{xx}, n_{zz}]$ [38]. From the figure, we find $L_\pi^{\text{aniso}} \sim 12\,\mu\text{m}$ at $\lambda = 1500\,\text{nm}$, in good agreement with Eq. (3), and observe that the beat length becomes significantly flatter with wavelength. From Fig. 3(b) we furthermore note that for variation of ± 10 % in the duty-cycle, n_{xx} and n_{zz} vary by approximately ± 10 %. These variation have, however, little impact on the beat length [see Fig. 3(a)], as they partially cancel out in Eq. 3. We thus opt for a duty-cycle of ~ 50 %, which facilitates fabrication, as it results in the largest linewidths for a given grating period.

It is noted that the precise dispersion behavior of the MMI modes near their Bragg wavelength can only be obtained in full 3D simulations, which enables us to further flatten the beat length by fine-tuning the pitch of the structure.

3. Design and simulation

We use full 3D simulations to assess and further optimize the performance of both the conventional and the sub-wavelength metamaterial engineered MMI. Figure 4 shows the simulated wavelength dependence of the beat length of a conventional MMI; the propagation constants $\beta_{1,2}$ were obtained with a commercial mode solver [39]. As expected from the 2D model [Fig. 3(a)], the beat length exhibits a strong variation with wavelength, between 35 μm and 23 μm, resulting in performance degratation when de-tuning the device from its design wavelenght. For a conventional MMI with the optimized dimensions shown in table 1, the simulated impact of this de-tuning is shown Fig. 5, including the excess losses (EL), imbalance (IB) and

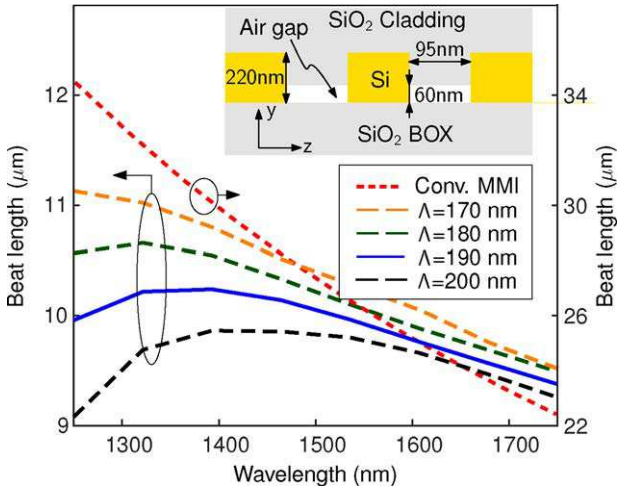

Figure 4 Full vectorial 3D simulations of beat length as a function of wavelength for a conventional MMI device (right scale) and the broadband MMI (left scale). With a judiciously designed pitch, the modal dispersion of the SWG structure in the broadband MMI further reduces the wavelength dependence of the beat length. Inset: Schematic side-view of the SWG in the broadband MMI showing small air gaps under the SiO_2 upper cladding. The geometric parameters of the device are given in table 1.

phase error (PE). By denoting the complex transmission from the fundamental mode of input waveguide 1 to the fundamental mode of the output waveguides 3 and 4 as s_{31} and s_{41} (see Fig. 1), these performance parameters are: $\text{EL} = 10\log(|s_{31}|^2 + |s_{41}|^2)$, $\text{IB} = 10\log(|s_{31}|^2/|s_{41}|^2)$, and $\text{PE} = \angle(s_{31}/s_{41}) - 90^\circ$. From Figs. 5(a)-(c) it is obvious that as the device is operated further away from its design wavelength its performance steadily deteriorates. Aiming for excess losses and imbalance below 1 dB and phase error smaller than 5° thus yields a bandwidth of under 200 nm for this optimized MMI design.

The wavelength dependence of the beat length in our sub-wavelength engineered MMI [see Fig. 2(a)] is shown, for a 50 % duty-cycle, in Fig. 4; the propagation constants $\beta_{1,2}$ were obtained using 3D Finite Difference Time Domain (FDTD) simulations [40], and the procedure described in [41]. For the device parameters given in table 1, we find that by fine-tuning the pitch near 190 nm, and thereby adjusting the dispersion of the MMI modes, the beat length becomes virtually wavelength independent in the 1250 nm to 1750 nm wavelength range. Furthermore, the beat length at $\lambda = 1500\,\text{nm}$ is $L_\pi^{\text{SWG}} \sim 10\,\mu\text{m}$, which is a threefold reduction compared to the conventional device.

In our initial design we assumed that the upper SiO_2 would completely fill the trenches between the silicon segments. However, kite-shaped air gaps with an area of $\sim 5700\,\text{nm}^2$ remain inside the trenches of the fabricated devices (see section 4). These gaps reduce the beat-length of the MMI by ~ 10 %, but do not affect its broadband performance. Since the gaps are very narrow (~ 45 nm) compared to the wavelength, their effect is governed mainly by their cross-sectional area, not their specific shape. We found

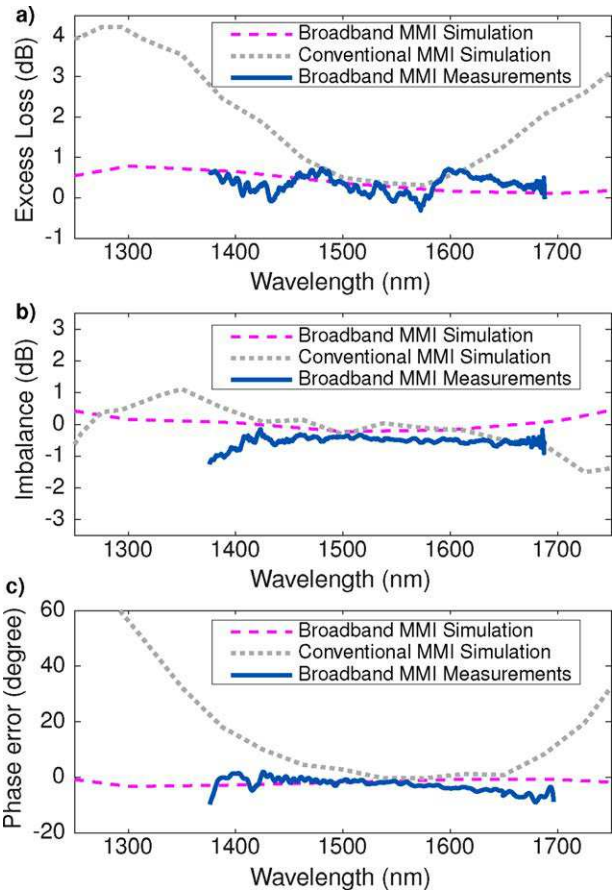

Figure 5 Measured and simulated performance of the broadband MMI compared to an optimized conventional MMI design, including a) excess loss, b) imbalance and c) phase error. The broadband coupler design shows high performance over a 500 nm bandwidth and the fabricated device has a measured bandwidth of 300 nm, while the conventional MMI design has a bandwidth of less than 200 nm and the footprint is three times larger.

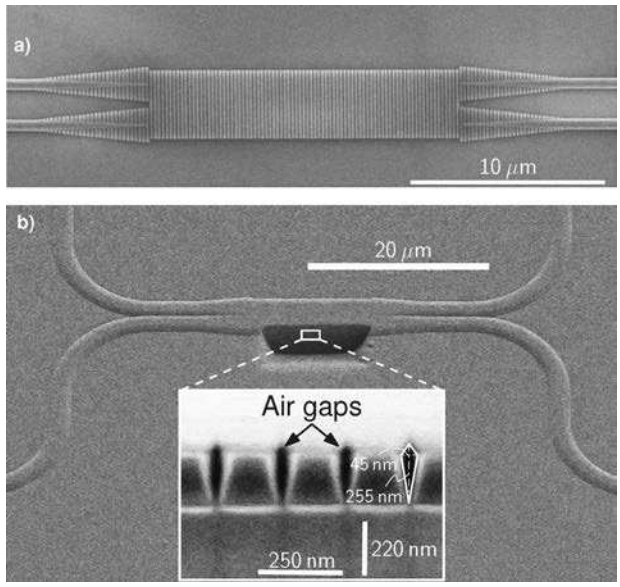

Figure 6 a) SEM image of a fabricated ultra-broadband MMI, prior to the deposition of the SiO_2 cladding. b) SEM image after the deposition of the cladding and a focused ion beam cut along the multimode region. The inset shows a tilted SEM image of the longitudinal cross-section of the device, revealing that kite-shaped air holes with an area of $\sim 5700\,\mathrm{nm}^2$ are present in the trenches.

that for simulation purposes they can be treated as rectangular holes of the same area ($95\,\mathrm{nm} \times 60\,\mathrm{nm} = 5700\,\mathrm{nm}^2$), as shown in the inset of Fig. 4. All 3D simulation results presented in this section and the next include this gap.

For a pitch of $\Lambda = 190\,\mathrm{nm}$ the wavelength averaged beat length is $L_\pi \approx 10\,\mu\mathrm{m}$, yielding a device with approximately $(3/2)L_\pi/\Lambda = 79$ periods for a 2×2 MMI device. The remaining geometrical parameters of the MMI [see Fig. 2(a)] are optimized following the design strategy described in [34], using initial design parameters provided by 2D simulations. We first set the width of the access waveguides to $W_A = 1.7\,\mu\mathrm{m}$ which ensures that only the guided modes are excited in the MMI region. We then chose the minimum separation between the input tapers ($s = 0.3\,\mu\mathrm{m}$) to avoid coupling between them. The length and width of the device were iteratively optimized using 3D-FDTD simulations of the complete structure that take into account material dispersion, yielding $W_{\mathrm{MMI}} = 3.25\,\mu\mathrm{m}$ and 74 SWG periods, respectively. Device performance for the optimized dimensions is shown in Fig. 5. These results confirm high-performance device operation over a 500 nm wavelength span, with excess losses and imbalance below 1 dB, and phase error less than 5°. This is an unprecedented almost threefold bandwidth enhancement compared to the conventional MMI.

In terms of fabrication tolerances, we found that in order to preserve this performance over the complete 500 nm bandwidth, the most critical parameters are the duty-cycle of the subwavelength structure, which has to be controlled to within ±7 %, and the MMI width, which should vary less than ±50 nm. A detailed analysis is included in the supporting information.

4. Experimental results

In order to experimentally validate the broadband operation of our device, we fabricated both individual MMIs, asymmetric Mach-Zehnder interferometers and reference waveguides on a standard 220 nm silicon-on-insulator wafer. To enable broadband light coupling to the chip we used sub-wavelength engineered fiber-to-chip mode transformers [27]. The devices were defined with electron beam lithography and transferred to the silicon layer with reactive ion etching. Figure 6(a) shows a Scanning Electron Microscope (SEM) image of one of the fabricated devices. The SiO_2 upper cladding was then deposited using plasma-enhanced chemical vapor deposition. A focussed ion beam cut and subsequent tilted SEM imaging revealed that the

oxide cladding only partially penetrated the trenches, leaving kite-shaped holes with an area of approximately 5700 nm^2, as shown in Fig. 6(b). Note that since silicon and silicon-dioxide are virtually indistinguishable in the SEM analysis, the $\sim$ 50 % silicon duty-cycle is not apparent in the image. The effect of the gaps is included in the simulations, as described in the previous section.

Measurements of the devices were carried out on two independent setups, with the input polarization set to quasi-TE (electric field in the horizontal plane) in both cases. To determine excess losses, the transmission through an individual MMI was normalized to the transmission through a reference waveguide. The phase error was obtained from the interferogram produced by the asymmetric Mach-Zehnder interferometers, using a minimum-phase technique [42].

An initial screening of the devices was carried out using a tunable laser source at the input and power detector at the output, covering the 1400 nm to 1600 nm range. We found that devices with a nominal duty-cycle of 50 % and a length around 74 periods exhibited the best performance, as predicted by the simulations. Figure 7 shows measurement results for devices with 72, 74 and 76 periods, i.e. for variations in the length of the multimode section of $\sim$ 3 %. While the excess loss of these three devices are essentially equal in the considered wavelength range [see Fig. 7(a)] and the phase errors are similar [see Fig. 7(c)] in terms of imbalance the 74 period long device is superior [see Fig. 7(b)].

In order to measure the 74 periods long device in an even broader wavelength range, we used a second setup with a broadband light source as input and an optical spectrum analyzer at the output. The measurement data from both setups was found to be in very good agreement in the common wavelength range, with a deviation below 5° in phase, 0.5 dB in imbalance and 1 dB in excess loss.

The experimental results shown in Fig. 5 reveal high device performance in the 1375 nm - 1700 nm wavelength range: excess losses and imbalance are below 1 dB, and the phase error is smaller than 5°, thereby confirming the broadband behavior of the device. We observed a resonant behavior near 1350 nm, which is attributed to an increased duty-cycle of the fabricated devices and could be addressed with proper pre-scaling of the mask. Our broadband source does not extend beyond 1700 nm preventing measurements at longer wavelengths.

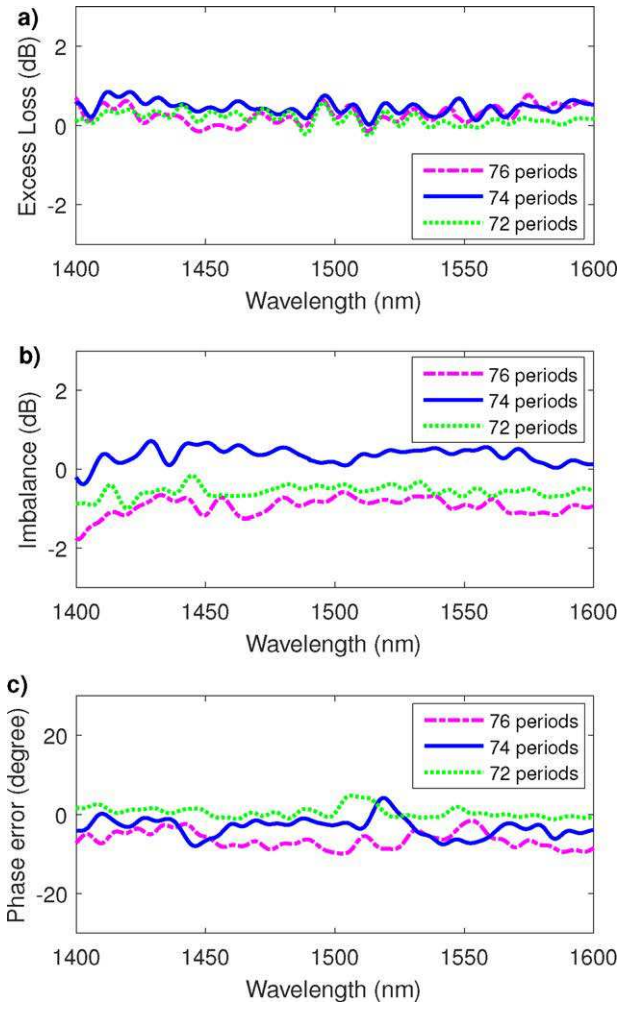

Figure 7 Measured excess loss (a), imbalance (b), and phase error (c) of three MMI with a different number of periods around the optimal value of 74. Neither excess loss nor phase error are strongly affected by the lengths variations, but the 76 periods long devices incurs a penalty of $\sim$ 1.2 dB in imbalance.

5. Conclusions

In conclusion, we have shown that the intrinsic anisotropy of sub-wavelength engineered metamaterials can be exploited to design compact and ultra-broadband nanophotonic beam splitters. Specifically, by controlling anisotropy and dispersion of a nanophotonic metamaterial waveguide, we have demonstrated MMI designs with high performance over a 500 nm bandwidth and have fabricated a device with a measured bandwidth in excess of 300 nm, showing a substantial improvement compared to conventional MMIs. We believe that this new strategy to engineer ultra-broadband waveguide devices can usher in broadband integrated nanophotonic systems with applications in coherent communications, sensing, spectroscopy and quantum photonics.

Supporting Information

Additional supporting information may be found in the online version of this article at the publisher's website.

Acknowledgements. We acknowledge funding from the Ministerio de Economía y Competitividad, Programa Estatal de Investigación, Desarrollo e Innovación Orientada a los Retos de la Sociedad (cofinanciado FEDER), Proyecto TEC2013-46917-C2-1-R, Proyecto TEC2016-80718-R, and the Universidad de Málaga. We would like to thank Dr. Jean Lapointe from NRC Canada for preparing files for e-beam lithography, and Dr. Xiaohua Wu from NRC Canada for his help with the focussed ion beam experiment.

Received: 15 August 2016, **Accepted:** 26 October 2016

Published online: 23 November 2016

Key words: anisotropy, broadband, multimode interference, silicon photonics.

References

[1] P. Dong, X. Liu, S. Chandrasekhar, L. L. Buhl, R. Aroca, and Y.-K. Chen, "Monolithic silicon photonic integrated circuits for compact 100 Gb/s coherent optical receivers and transmitters", IEEE J. Sel. Top. Quantum Electron. **20**(4), 150–157 (2014).

[2] A. Sano, T. Kobayashi, S. Yamanaka, A. Matsuura, H. Kawakami, Y. Miyamoto, K. Ishihara, and H. Masuda, "102.3-Tb/s (224 × 548-Gb/s) C-and extended L-band all-Raman transmission over 240 km using PDM-64QAM single carrier FDM with digital pilot tone", in *National Fiber Optic Engineers Conference*. Optical Society of America, 2012, pp. PDP5C–3.

[3] M.-C. Estevez, M. Alvarez, and L. M. Lechuga, "Integrated optical devices for lab-on-a-chip biosensing applications", Laser Photonics Rev. **6**(4), 463–487 (2012).

[4] D. Rodrigo, O. Limaj, D. Janner, D. Etezadi, F. J. G. de Abajo, V. Pruneri, and H. Altug, "Mid-infrared plasmonic biosensing with graphene", Science **349**(6244), 165–168 (2015).

[5] M. Nedeljkovic, A. V. Velasco, A. Z. Khokhar, A. Delâge, P. Cheben, and G. Z. Mashanovich, "Mid-infrared silicon-on-insulator fourier-transform spectrometer chip", IEEE Photonic Tech. L. **28**(4) 528–531 (2016).

[6] E. LeCoarer, S. Blaize, P. Benech, I. Stefanon, A. Morand, G. Lérondel, G. Leblond, P. Kern, J. M. Fedeli, and P. Royer, "Wavelength-scale stationary-wave integrated fourier-transform spectrometry", Nat. Photonics **1**(8), 473–478 (2007).

[7] A. Pasquazi, M. Peccianti, Y. Park, B. E. Little, S. T. Chu, R. Morandotti, J. Azaña, and D. J. Moss, "Sub-picosecond phase-sensitive optical pulse characterization on a chip", Nat. Photonics **5**(10), 618–623 (2011).

[8] L. Razzari, D. Duchesne, M. Ferrera, R. Morandotti, S. Chu, B. Little, and D. Moss, "CMOS-compatible integrated optical hyper-parametric oscillator", Nat. Photonics **4**(1), 41–45 (2010).

[9] A. Crespi, R. Osellame, R. Ramponi, V. Giovannetti, R. Fazio, L. Sansoni, F. DeNicola, F. Sciarrino, and P. Mataloni, "Anderson localization of entangled photons in an integrated quantum walk", Nat. Photonics **7**(4), 322–328 (2013).

[10] J. He, B. A. Bell, A. Casas-Bedoya, Y. Zhang, A. S. Clark, C. Xiong, and B. J. Eggleton, "Ultracompact quantum splitter of degenerate photon pairs", Optica **2**(9), 779–782 (2015).

[11] H. F. Talbot, "Facts relating to optical science", Philos. Mag. **9**(4), 401–407 (1836).

[12] R. Ulrich and G. Ankele, "Self-imaging in homogeneous planar optical waveguides", Appl. Phys. Lett. **27**, 337–339 (1975).

[13] L. B. Soldano and E. Pennings, "Optical multi-mode interference devices based on self-imaging: principles and applications", J. Lightwave Technol. **13**(4), 615–627, (1995).

[14] P. Runge, S. Schubert, A. Seeger, K. Janiak, J. Stephan, D. Trommer, P. Domburg, and M. L. Nielsen, "Monolithic InP receiver chip with a 90° hybrid and 56 GHz balanced photodiodes", Opt. Express **20**(26), B250–B255 (2012).

[15] R. Halir, G. Roelkens, A. Ortega-Mo nux, and J. G. Wangüemert-Pérez, "High-performance 90° hybrid based on a silicon-on-insulator multimode interference coupler", Opt. Lett. **36**(2), 178–180 (Jan 2011).

[16] Y. Zhang, A. Hosseini, X. Xu, D. Kwong, and R. T. Chen, "Ultralow-loss silicon waveguide crossing using Bloch modes in index-engineered cascaded multimode-interference couplers", Opt. Lett. **38**(18), 3608–3611 (Sep 2013).

[17] E. Kleijn, M. Smit, and X. Leijtens, "Multimode interference reflectors: A new class of components for photonic integrated circuits", J. Lightwave Technol. **31**(18), 3055–3063 (Sep 2013).

[18] J. S. Fandiño, J. D. Doménech, and P. Muñoz, "Two-port multimode interference reflectors based on aluminium mirrors in a thick SOI platform", Opt. Express **23**(16), 20219–20233 (Aug 2015).

[19] M. Tajaldini and M. Jafri, "Simulation of an ultra-compact multimode interference power splitter based on kerr nonlinear effect", J. Lightwave Technol. **32**(7), 1282–1289 (April 2014).

[20] Z. Zhu, C. E. Garcia-Ortiz, Z. Han, I. P. Radko, and S. I. Bozhevolnyi, "Compact and broadband directional coupling and demultiplexing in dielectric-loaded surface plasmon polariton waveguides based on the multimode interference effect", Appl. Phys. Lett. **103**(6), 061108 (2013).

[21] X. Guan, H. Wu, Y. Shi, and D. Dai, "Extremely small polarization beam splitter based on a multimode interference coupler with a silicon hybrid plasmonic waveguide", Opt. Lett. **39**(2), 259–262 (2014).

[22] R. Zheng, D. Gao, and J. Dong, "Ultra-compact broadband tunable graphene plasmonic multimode interferometer", IEEE Photonic Tech. L. **28**, 645–648 (2016).

[23] P. A. Besse, M. Bachmann, H. Melchior, L. B. Soldano, and M. K. Smit, "Optical bandwidth and fabrication tolerances of multimode interference couplers", J. Lightwave Technol. **12** (6), 1004–1009 (1994).

[24] H. Kikuta, Y. Ohira, and K. Iwata, "Achromatic quarter-wave plates using the dispersion of form birefringence", Appl Opt **36** (7), 1566–1572 (1997).

[25] P. Cheben, P. J. Bock, J. H. Schmid, J. Lapointe, S. Janz, D.-X. Xu, A. Densmore, A. Delâge, B. Lamontagne, and T. J. Hall, "Refractive index engineering with subwavelength gratings for efficient microphotonic couplers and planar waveguide multiplexers", Opt. Lett. **35**(15), 2526–2528 (2010).

[26] R. Halir, P. J. Bock, P. Cheben, A. Ortega-Moñux, C. Alonso-Ramos, J. H. Schmid, J. Lapointe, D.-X. Xu, J. G. Wangüemert-Pérez, Í. Molina-Fernández *et al.*, "Waveguide sub-wavelength structures: a review of principles and applications", Laser Photonics Rev. **9**(1), 25–49 (2015).

[27] P. Cheben, J. H. Schmid, S. Wang, D.-X. Xu, M. Vachon, S. Janz, J. Lapointe, Y. Painchaud, and M.-J. Picard, "Broadband polarization independent nanophotonic coupler for silicon waveguides with ultra-high efficiency", Opt. Express **23**(17), 22553–22563 (Aug 2015).

[28] D. Benedikovic, P. Cheben, J. H. Schmid, D.-X. Xu, B. Lamontagne, S. Wang, J. Lapointe, R. Halir, A. Ortega-Moñux, S. Janz, and M. Dado, "Subwavelength index engineered surface grating coupler with sub-decibel efficiency for 220-nm silicon-on-insulator waveguides", Opt. Express **23**(17), 22 628–22 635 (Aug 2015).

[29] A. Y. Piggott, J. Lu, K. G. Lagoudakis, J. Petykiewicz, T. M. Babinec, and J. Vučković, "Inverse design and demonstration of a compact and broadband on-chip wavelength demultiplexer", Nat. Photonics **9**(6), 374–377 (2015).

[30] B. Shen, P. Wang, R. Polson, and R. Menon, "An integrated-nanophotonics polarization beamsplitter with $2.4 \times 2.4\,\mu m^2$ footprint", Nat. Photonics **9**(6), 378–382 (2015).

[31] A. Ortega-Moñux, C. Alonso-Ramos, A. Maese-Novo, R. Halir, L. Zavargo-Peche, D. Pérez-Galacho, I. Molina-Fernández, J. G. Wangüemert-Pérez, P. Cheben, J. H. Schmid *et al.*, "An ultra-compact multimode interference coupler with a subwavelength grating slot", Laser Photonics Rev. **7**(2), L12–L15 (2013).

[32] A. Maese-Novo, R. Halir, S. Romero-García, D. Pérez-Galacho, L. Zavargo-Peche, A. Ortega-Moñux, I. Molina-Fernández, J. Wangüemert-Pérez, and P. Cheben, "Wavelength independent multimode interference coupler", Opt. Express **21**(6), 7033–7040, (2013).

[33] C.-L. Chen, Foundations for Guided-Wave Optics (Wiley, 2006).

[34] R. Halir, I. Molina-Fernández, A. Ortega-Moñux, J. Wangüemert-Pérez, D.-X. Xu, P. Cheben, and S. Janz, "A design procedure for high-performance, rib-waveguide-based multimode interference couplers in silicon-on-insulator", J. Lightwave Technol. **26**(16), 2928–2936 (2008).

[35] B. Saleh and M. Teich, Fundamentals of Photonics, J. W. Goodman, Ed. (Wiley, 1991), chapter 6.

[36] C. Gu and P. Yeh, "Form birefringence dispersion in periodic layered media", Opt. Lett. **21**(7), 504–506 (1996).

[37] G. Bouchitte and R. Petit, "Homogenization techniques as applied in the electromagnetic theory of gratings", Electromagnetics **5**(1), 17–36 (1985).

[38] Y. Satomura, M. Matsuhara, and N. Kumagai, "Analysis of electromagnetic-wave modes in anisotropic slab waveguide", IEEE T. Microw. Theory **22** (2), 86–92 (1974).

[39] "Fimmwave & Fimmprop, available from Photon Design, https://www.photond.com.

[40] "Fullwave, available from RSoft, http://www.rsoftdesign.com.

[41] J. G. Wangüemert-Pérez, P. Cheben, A. Ortega-Moñux, C. Alonso-Ramos, D. Pérez-Galacho, R. Halir, Í. Molina-Fernández, D.-X. Xu, and J. H. Schmid, "Evanescent field waveguide sensing with subwavelength grating structures in silicon-on-insulator", Opt. Lett. **39**(15), 4442–4445 (Aug 2014).

[42] R. Halir, I. Molina-Fernández, J. Wangüemert-Pérez, A. Ortega-Moñux, J. de Oliva-Rubio, and P. Cheben, "Characterization of integrated photonic devices with minimum phase technique", Opt. Express **17**(10), 8349–8361 (2009).